



Controlling of cellular substructure and its effect on mechanical properties of FeCoCrNiMo_{0.2} high entropy alloy fabricated by selective laser melting

Ao Fu^a, Zhonghao Xie^a, Jian Wang^a, Yuankui Cao^{a, **}, Bingfeng Wang^{a,b}, Jia Li^c, Qihong Fang^c, Xiaofeng Li^d, Bin Liu^{a,*}, Yong Liu^a

^a State Key Laboratory of Powder Metallurgy, Central South University, Changsha, 410083, China

^b School of Materials Science and Engineering, Central South University, Changsha, 410083, China

^c State Key Lab of Advanced Design and Manufacturing for Vehicle Body, Hunan University, Changsha, 410082, China

^d School of Materials Science and Engineering, North University of China, Taiyuan, 030051, China



ARTICLE INFO

Keywords:

High entropy alloy
Selective laser melting
Microstructure
Mechanical property

ABSTRACT

Fine cellular substructures are typical microstructure feature of high entropy alloys (HEAs) produced via selective laser melting (SLM), playing a pivotal role in improving the mechanical properties. Nonetheless, the controlling of cellular substructure and its impact on the mechanical properties remains ambiguous. This study investigates the effect of energy densities on the cellular substructure evolution and mechanical properties of the FeCoCrNiMo_{0.2} HEA. It is found the increase in energy density causes a decrease in temperature gradient (G) and solidification rate (R) in molten pool, consequently leading to the increase of cellular substructure size and the intensification of Mo segregation at cellular substructure boundaries. The cellular substructure size (d) can be described by formula $d = 80(GR)^{-1/3}$, in which G and R can be obtained from discrete element method - computational fluid dynamics (DEM-CFD) simulation. The strength of the FeCoCrNiMo_{0.2} HEA is significantly affected by dislocation strengthening (σ_d) and segregation strengthening (σ_s), which are further determined by the cellular substructure size and the Mo segregation, respectively. The increase of cellular substructure size leads to the decrease of σ_d , while the intensification of Mo segregation results in the increase of σ_s . The competition between these two strengthening effects leads to an optimized and excellent tensile property of 707 MPa in yield strength, 947 MPa in ultimate tensile strength and 34 % in fracture elongation at a moderate energy density of 47 J/mm³. The findings provide guidance towards the advancement of high-performance high entropy alloys fabricated by SLM in terms of cellular substructure controlling.

1. Introduction

Additive manufacturing (AM) has attracted a lot of attention in the global manufacturing industries because it provides an unparalleled capability for achieving near-net-shape production of intricately shaped engineering components that are not attainable through traditional fabrication methods [1–5] such as casting, rolling, forging, extrusion, etc. Owing to these advantages, AM is now widely used to fabricate a wide range of metallic materials, including steels [6], nickel-based superalloys [7], titanium alloys [8], aluminum alloys [9], and its application in modern industries continues to expand.

As one of the widely adopted AM methods, selective laser melting (SLM) has an ultrahigh cooling rate (10^6 – 10^8 K/s [10–13]), which can

not only effectively inhibit the precipitation of harmful secondary phases in the casted materials that usually form at intermediate or high temperatures [10], but also promote the formation of fine cellular substructures [12,13], strongly enhancing the mechanical properties. For example, Brif et al. [14] found that the yield strength of the SLMed FeCoCrNi high entropy alloy (HEA) can even reach more than three times than that prepared by arc melting (188 MPa), and it also has a good elongation (>30%). Liu et al. [15] reported that the SLMed 316L austenitic stainless steel (SS) shows superior tensile yield strength and elongation combination (590 MPa, 36 %) than that of the traditional 316L SS (160 MPa, 43 %). Zhu et al. [12] successfully fabricated a near-fully dense FeCoCrNiMn HEA by SLM. The tensile yield strength reaches 510 MPa, which is nearly doubles compared with the casting

* Corresponding author.

** Corresponding author.

E-mail addresses: caoyuankui@csu.edu.cn (Y. Cao), binliu@csu.edu.cn (B. Liu).

state (210 MPa), while the elongation is still as high as 40 %. The high strength for the AMed materials is mainly owing to the fine cellular substructures formed through the rapid solidification process, which can act as a low angle grain boundaries to hinder the dislocation motion and increase the dislocation storage. In addition, recent studies reported that the segregation of solute atoms, such as Cr and Mo, is prone to occur at the cellular substructure boundaries [10,15,16], further enhancing mechanical properties. For instance, Smith et al. [17] found that the presence of obvious Cr segregation at the cellular substructure boundaries in the AMed 304L SS, and the strength contribution from composition segregation can reach 123–135 MPa. Li et al. [18] reported that Mo also easily segregates at the cellular substructure boundaries of the FeCoCrNi HEA, which can lead to an increased strength of 338.6 MPa. Therefore, it is of great significance to optimize the mechanical properties of the AMed alloys by regulating the morphological features and composition segregation of cellular substructures. In our previous study, we reported a FeCoCrNiMo_{0.2} HEA with excellent mechanical properties [4], and now are trying to prepare the HEA by SLM. However, the microstructural evolution of cellular substructures and its regulation mechanism remain unclear so far.

In this work, we further studied the effect of the SLM process on the cellular substructure size and the element segregation behavior at cellular substructure boundaries of the SLMed FeCoCrNiMo_{0.2} HEA. The reason for choosing a Mo-contained HEA is mainly because the equilibrium distribution coefficient of Mo element is greater than that of Cr element [19,20]. This will lead to more obvious composition segregation at the cellular substructure boundaries, which is beneficial to the study of segregation behavior at the cellular substructure boundaries. The FeCoCrNiMo_{0.2} HEA was prepared by SLM, and the effect of SLM process parameters (scanning speed, laser power, and hatch spacing) on the morphology features and elemental segregation of cellular substructures was investigated. The goal of this work is to clarify the microstructural evolution of cellular substructures and reveal its influence on the mechanical properties.

2. Materials and methods

Gas-atomized FeCoCrNiMo_{0.2} HEA powders were adopted as the raw materials for SLM, with an average particle size of ~67.1 μm. Fig. 1a

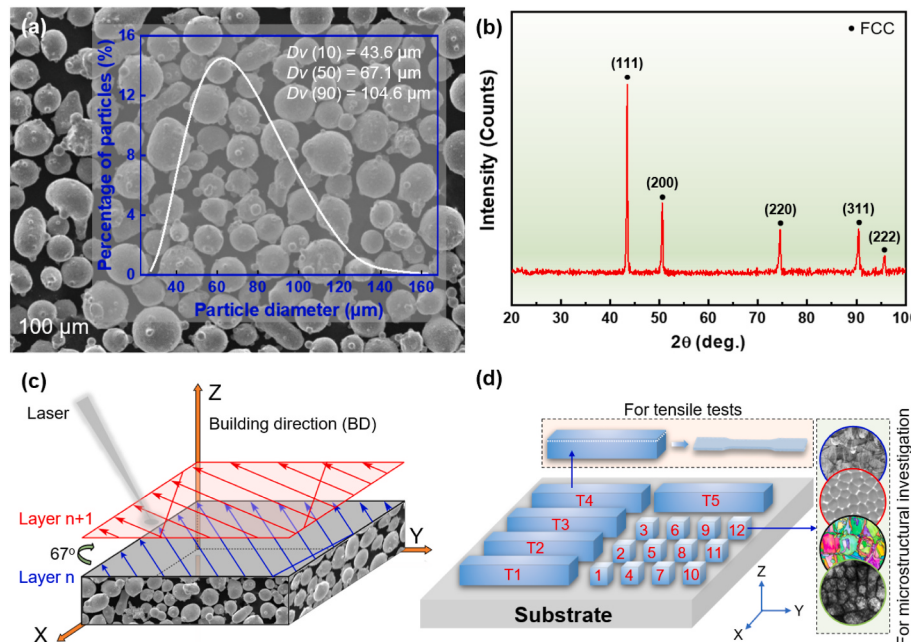


Fig. 1. (a) Powder morphology, particle size distribution, and (b) phase composition of the gas-atomized FeCoCrNiMo_{0.2} HEA powders; schematic diagram of (c) laser scanning strategy and (d) SLMed samples.

shows the SEM image of the powder morphology, which mainly have a near-spherical shape. The XRD patterns in Fig. 1b reveals that the gas-atomized powders are in a single face-centered-cubic (FCC) structure. In addition, the chemical composition of the powders was analyzed by inductively coupled plasma mass spectroscopy (ICP-MS), and the result is listed in Table 1.

SLMed samples were fabricated using an FS273 M machine (Farsoon, China) equipped with a YAG fiber laser, which has a maximum output power of 500 W and a laser beam diameter of 90 μm. Before initiating the selective laser melting (SLM) process, the chamber of the SLM machine underwent vacuuming and subsequent filling with high-purity argon gas, ensuring a low oxygen content of less than 100 ppm. Table 2 shows the detail of SLM process parameters used in this work to determine the range of parameters applicable to the SLMed FeCoCrNiMo_{0.2} HEA. A single variable of each group of parameters is selected to explore the impacts of different SLM process parameters on both microstructure and mechanical properties, as shown in Table 3. In AM techniques, the energy density the energy density serves as a linkage between process parameters [21], expressed as $E = P/vhd$, where E, P, v, h and d represent the energy density (J/mm^3), laser power (W), scanning speed (mm/s), hatch spacing (mm) and layer thickness (mm), respectively. Cube-shaped samples (10 mm × 10 mm × 8 mm) and sheet-shaped samples (70 mm × 12 mm × 8 mm) were built for microstructural observation and mechanical test, respectively (Fig. 1d). All the SLM samples were annealed at 400 °C in a vacuum furnace for 3 h with a subsequent furnace cool to mitigate residual internal stress. Sample density was measured according to the Archimedes method. As illustrated in Fig. 2, the relative densities range from about 91.09 % to 99.85 %, which increases obviously with energy densities in the range of 31–47 J/mm³, but almost keeps stable in the range of 47–94 J/mm³. With the energy densities further increasing to 150 J/mm³, the relative density decreases to 98.19 %, which is mainly because the excess energy

Table 1
Chemical composition of the FeCoCrNiMo_{0.2} HEA powders (at.%).

Elements	Fe	Co	Cr	Ni	Mo
Powders	23.93	23.68	23.82	23.76	4.81

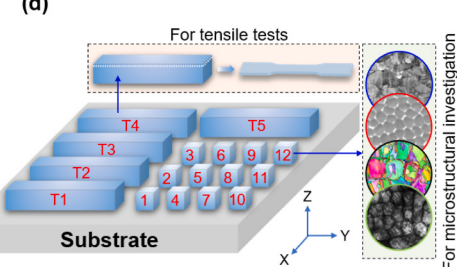


Table 2
SLM process parameters for the FeCoCrNiMo_{0.2} HEA.

Process parameter	Definition	Value
Laser power (P , W)	Laser input energy for hatching tracks	150–450
Scanning speed (V , mm/s)	Scanning speed of the laser for hatching tracks	400–1000
Layer thickness (t , mm)	Downward movement of the base plate between layers	0.06
Hatch spacing (h , mm)	Distance between adjacent laser tracks	0.05–0.2
Scanning strategy	Stripe scanning/Subarea scanning	–
Stripe width (mm)	Width of blocking area	10
Angle shift (°)	Pattern rotation between layers	67
Build plate temperature (°C)	Temperature preset of the build plate	100

Table 3
SLM process parameters for optimizing the microstructure of the FeCoCrNiMo_{0.2} HEA.

Laser power (P , W)	Scanning speed (V , mm/s)	Hatch spacing (h , mm)	Layer thickness (t , mm)	Energy density (E , J/mm ³)
280	400	0.1	0.06	117
280	600	0.1	0.06	78
280	800	0.1	0.06	58
280	1000	0.1	0.06	47
150	800	0.1	0.06	31
330	800	0.1	0.06	69
360	800	0.1	0.06	75
400	800	0.1	0.06	83
450	800	0.1	0.06	94
360	800	0.05	0.06	150
360	800	0.15	0.06	50
360	800	0.2	0.06	38

easily leads to obvious splashing and formation of residual keyholes [22].

Phase composition was determined using X-ray diffraction analysis (XRD, D/MAX-2250) with Cu K α radiation. Microstructural analysis employed optical microscopy (OM, DM4000 M), scanning electron microscopy (SEM, Helios nanolab G3 UC) equipped with a backscattering electron diffraction (EBSD) detector, and transmission electron microscopy (TEM, Talos F200X) equipped with an energy-dispersive spectrometer (EDS). For microstructural examination, samples underwent electro-polishing in a solution composed of 60 % methanol, 34 % n-butyl alcohol, and 6 % perchloric acid at an applied DC voltage of 20 V. Average size of cellular substructure with different energy densities was analyzed by ImageJ Analysis Software. Tensile tests were performed on an Instron 3369 machine at room temperature, maintaining a constant strain rate of 1×10^{-3} s $^{-1}$, with the tensile direction oriented perpendicular to the building direction. Each tensile test was repeated at least three times to ensure the reliability of the obtained data.

In order to reveal the details of the microstructural evolution during the solidification process in the molten pool, a simulation of the temperature field distribution was conducted using the discrete element method - computational fluid dynamics (DEM-CFD) [11]. Here, a randomly distributed packed powder bed was first established by the DEM (Fig. 3a). The thermophysical parameters of the raw material were then calculated by JMatPro software, and the temperature field distribution in the molten pool was finally solved through Flow 3d software. The temperature gradient and cooling rate are taken from the average values in the center area of the molten pool, as shown in Fig. 3b.

3. Results

Fig. 4 exhibits the XRD patterns of the SLMed FeCoCrNiMo_{0.2} HEA under different energy densities, indicating that all the SLMed samples still maintain a single-phase FCC structure from its powder state. With the increase of energy densities from 31 J/mm³ to 150 J/mm³, the position of diffraction peak does not change obviously, indicating that there are no other secondary phases form during the SLM process. Significantly, the intensity of the (111) peak in the gas-atomized powders is more pronounced compared to the (200) and (220) peaks. The relative intensity of the latter two diffraction peaks increases gradually with increasing energy density, which means the appearance of preferred orientations. Apparently, the crystal growth directions in the SLM process are notably influenced by the energy density [12,23].

Fig. 5 shows representative microstructure of the SLMed FeCoCrNiMo_{0.2} HEA along building direction (XZ) and vertical building direction (XY). It can be found that the SLMed sample exhibits a typical hierarchical microstructure with coarse molten pools, micron grains and submicron cellular substructures. In the XY plane, staggered molten pool tracks with an angle of 67° can be observed (Fig. 5a), which is mainly due to the rotational scanning strategy employed during the SLM process. In the XZ plane, the microstructure presents a fish scale morphology (Fig. 5a and b), which is composed of numerous parallel molten pools. Coarse grains can be seen inside the molten pools (Fig. 5c), which will be described later in the following paragraph. Fig. 5d shows the high-magnification view in the molten pools, and it can be found that there are a large number of fine cellular substructures. The 3D structure of the cellular substructures is similar to the honeycomb structure, and morphology of the cellular substructures is depending on the observation direction [24], with a tubular morphology along the solidification direction and a cellular morphology perpendicular to the solidification direction.

Fig. 6 depicts the EBSD results of the SLMed FeCoCrNiMo_{0.2} HEA under energy densities of 47 J/mm³, 78 J/mm³ and 150 J/mm³. The inverse pole figure (IPF) maps in Fig. 6a shows that the grain orientation of the sample with energy density of 47 J/mm³ is randomly distributed. At a higher energy density of 150 J/mm³, most of the grains show a preferential orientation along <001> (Fig. 6c). Meanwhile, the maximum texture index of {001} plane in the XY view increases from

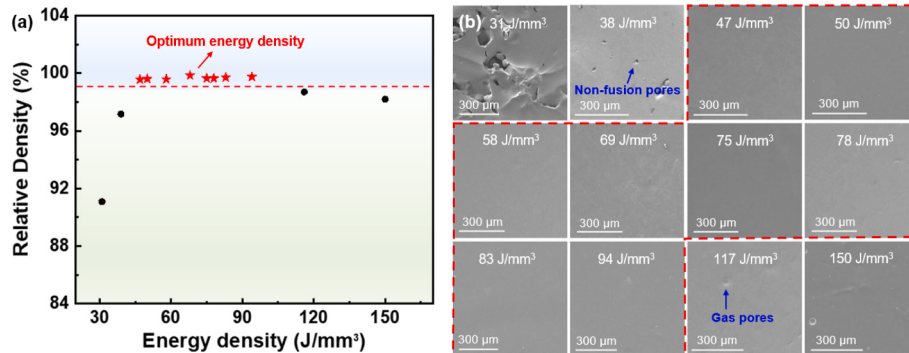


Fig. 2. Variation of (a) relative density and (b) porosity of the FeCoCrNiMo_{0.2} HEA under different energy densities.

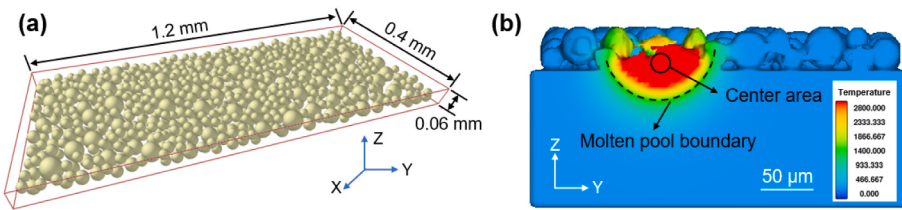


Fig. 3. Simulation of (a) powder bed and (b) temperature field distribution in the molten pool.

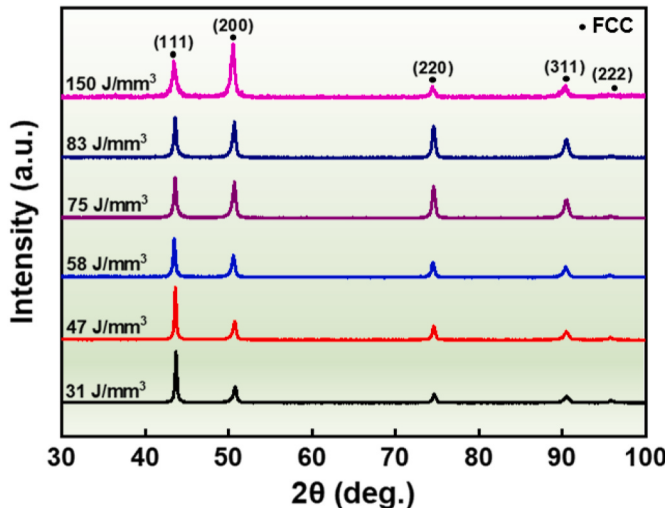


Fig. 4. XRD patterns of the FeCoCrNiMo_{0.2} HEA under different energy density.

1.99 to 5.03. This means that there is a growth texture of <100> in the samples with high energy densities, which is consistent with the XRD results. Fig. 6a1–c1 show the phase maps superimposed with high angle grain boundaries (HAGBs) and low angle grain boundaries (LAGBs). With an increase in energy density from 47 J/mm³ to 150 J/mm³, there is a notable reduction in the quantity of LAGBs and HAGBs, accompanied by an enlargement in grain size from 16.1 μm to 20.4 μm. This grain coarsening and equiaxed-to-dendritic transition is affected by the thermal gradients and cooling rates [10], which are closely related to the energy density. Fig. 6a2–c2 show Kernel average misorientation (KAM) maps, which exhibit high local misorientation, indicating that there are a large number of geometric necessary dislocations (GND). At an energy density of 47 J/mm³, the average local misorientation value is 1.53°. When the energy density increases to 150 J/mm³, the average local

misorientation decreases to 0.89°. The KAM value serves as an indicator of local misorientation and lattice mismatch, and the higher KAM value is believed to produce stronger dislocation strengthening [25].

Fig. 7 exhibits the SEM images of the cellular substructures in the SLMed FeCoCrNiMo_{0.2} HEA with different energy densities. It can be found, by increasing energy densities from 31 J/mm³ to 150 J/mm³, the cellular substructure size rises from 0.24 μm to 0.98 μm. Fig. 8a–c summarizes the changes of cellular substructure size under the following three parameters: scanning speed, laser power, and hatch spacing. Upon the scanning speed's increase from 400 mm/s to 1000 mm/s, the cellular substructure size decreases from 0.88 μm to 0.43 μm. Conversely, with an increase in laser power from 150 W to 450 W, the cellular substructure size increases from 0.24 μm to 0.84 μm. Additionally, as the hatch spacing increases from 0.05 mm to 0.2 mm, the cellular substructure size decreases from 0.98 mm to 0.36 mm. The variation of cellular substructure size with the energy density is also summarized in Fig. 8d, and the cellular substructure size shows a positive correlation with the energy density.

Fig. 9 depicts the element distribution of the SLMed FeCoCrNiMo_{0.2} HEA under energy density of 47 J/mm³, 78 J/mm³ and 150 J/mm³, indicating that main elements, including Fe, Co, Cr, Ni, are uniformly distributed in the cellular substructures. However, the concentration of Ni increases slightly at the cellular substructure boundaries, while other three elements show the opposite tendency. Special attention should be paid that Mo is mainly segregated at the cellular substructure boundaries, but is depleted inside the cellular substructures. TEM EDS was employed to measure the concentration of Mo at the cellular substructure boundaries and inside the cellular substructures, which are detailed in Table 4. The average difference of Mo concentration at the cellular substructure boundaries and within the cellular structures for the SLMed samples under energy density of 47 J/mm³, 78 J/mm³ and 150 J/mm³ are 1.89 at.%, 2.12 at.%, 2.31 at.%, respectively.

Fig. 10a summarizes the relationship between the energy density with tensile strength, cellular substructure size, and porosity of the SLMed FeCoCrNiMo_{0.2} HEA. The results reveals that the tensile strength of the SLMed samples is intricately associated with the cellular

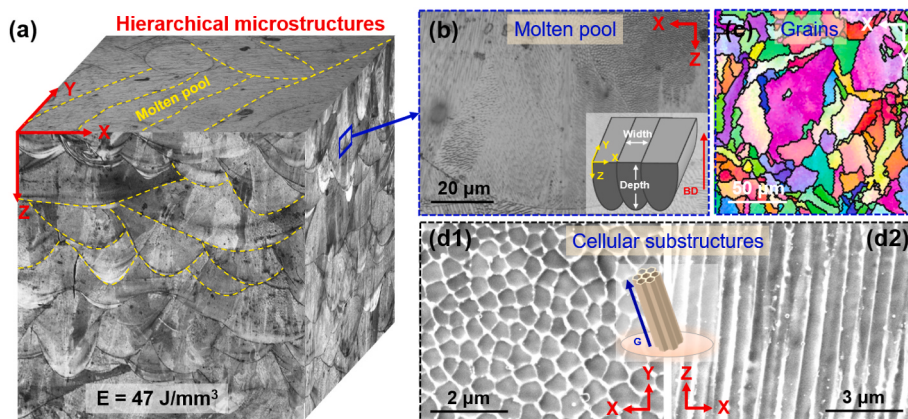


Fig. 5. (a) 3D SEM images of the FeCoCrNiMo_{0.2} HEA under energy density of 47 J/mm³. High-magnification view of (b) molten pools, (c) coarse grains, and (d) cellular substructures.

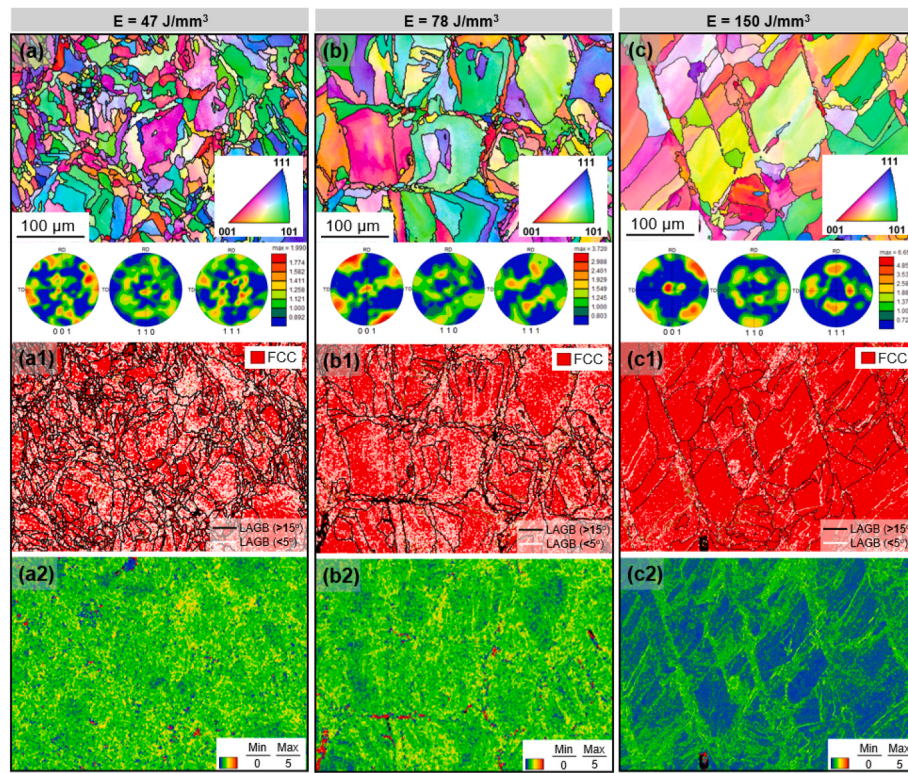


Fig. 6. EBSD results of the FeCoCrNiMo_{0.2} HEA under energy densities of 47 J/mm³, 78 J/mm³ and 150 J/mm³ (a–c) IPF maps, (a1–c1) phase maps superimposed with HAGBs and LAGBs, and (a2–c2) KAM maps.

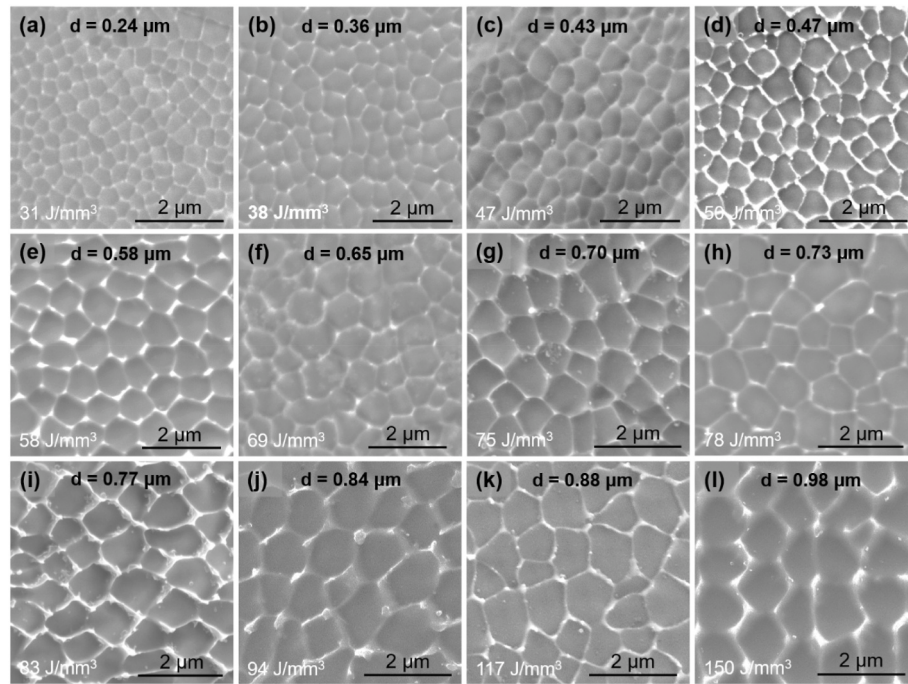


Fig. 7. SEM images of the FeCoCrNiMo_{0.2} HEA under different energy densities. (a) 31 J/mm³, (b) 38 J/mm³, (c) 47 J/mm³, (d) 50 J/mm³, (e) 58 J/mm³, (f) 69 J/mm³, (g) 75 J/mm³, (h) 78 J/mm³, (i) 83 J/mm³, (j) 94 J/mm³, (k) 117 J/mm³, (l) 150 J/mm³.

substructure size and porosity. At a low energy density of 31 J/mm³, the cellular substructure size, porosity, and tensile strength are 0.24 μm, 8.9 %, and 811 MPa, respectively. When the energy density increases to 47 J/mm³, the porosity of the SLMed sample rapidly drops to 0.43 %, while also possessing a small cellular substructure size of 0.43 μm. The SLMed

sample maintains a maximum tensile strength of 947 MPa. At this stage, the porosity stands out as the primary factor influencing the mechanical properties of SLMed samples. When the energy density is between 47 J/mm³ and 94 J/mm³, the SLMed samples have similarly low porosity, but their cellular substructure size increases significantly from 0.43 μm to

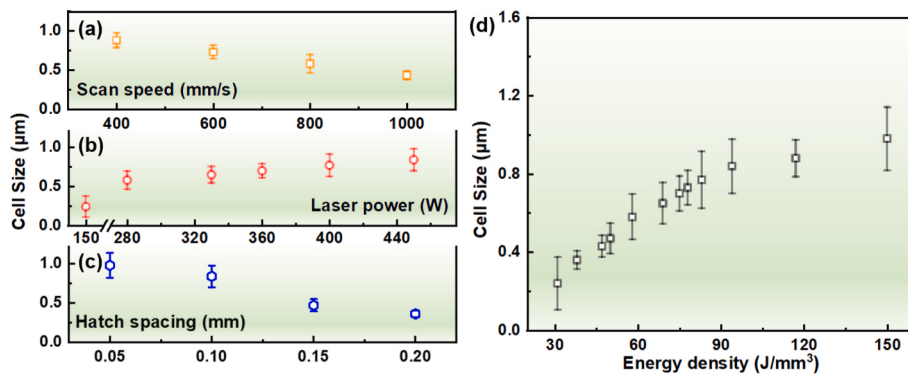


Fig. 8. Variation of cellular substructure size under different (a) scanning speed, (b) laser power, (c) hatch spacing, and (d) energy density.

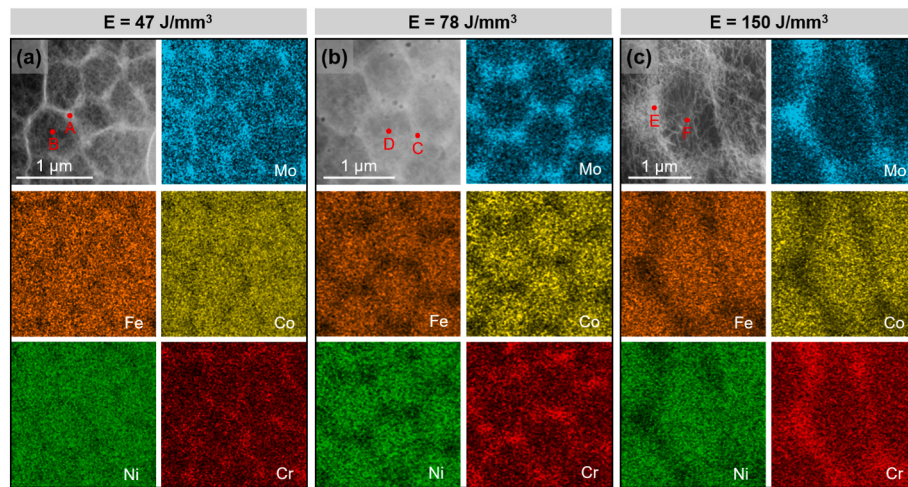


Fig. 9. EDS results of the FeCoCrNiMo_{0.2} HEA under energy density of 47 J/mm³, 78 J/mm³ and 150 J/mm³.

Table 4
Chemical composition inside and outside the cellular substructures (at.%).

Element	Point A	Point B	Point C	Point D	Point E	Point F
Mo	6.84	4.95	6.89	4.77	7.02	4.71

0.84 μm. Correspondingly, the tensile strength decreases from 947 MPa to 897 MPa. Further increasing the energy density to 150 J/mm³, the porosity and cellular substructure size increases to 1.8 % and 0.98 μm, respectively, while the tensile strength decreases to 878 MPa. Fig. 10b exhibits the tensile engineering stress-strain curves of the SLMed FeCoCrNiMo_{0.2} HEA under energy density from 47 J/mm³ to 150 J/mm³, and the details of tensile properties are summarized in Table 5. When the energy density is 47 J/mm³, the yield strength, tensile strength and elongation are 707 MPa, 947 MPa and 34 %, respectively,

showing an excellent combination of strength and ductility. As the energy density increases to 150 J/mm³, the mechanical properties drop to 638 MPa, 878 MPa and 28 %. Fig. 10c shows the strength-ductility combination of the SLMed FeCoCrNiMo_{0.2} HEA and other typical structural materials such as as-cast FeCoCrNiMo_{0.2} HEA, SLMed SSs, and SLMed HEAs/MEAs [12,14,26–40]. It can be found that compared with the SLMed SSs and SLMed HEAs/MEAs, the SLMed FeCoCrNiMo_{0.2} HEA highlighted by the red star shows a better combination of strength and ductility.

To understand the deformation mechanisms of the SLMed FeCoCrNiMo_{0.2} HEA, the microstructure of the fractured samples at the energy density of 47 J/mm³ was analyzed using EBSD and TEM. The EBSD results in Fig. 11a and b can be clearly reveal that the plastic deformation is mainly accommodated by dislocation activities and mechanical twins, and the coarse grains are significantly refined. The details of

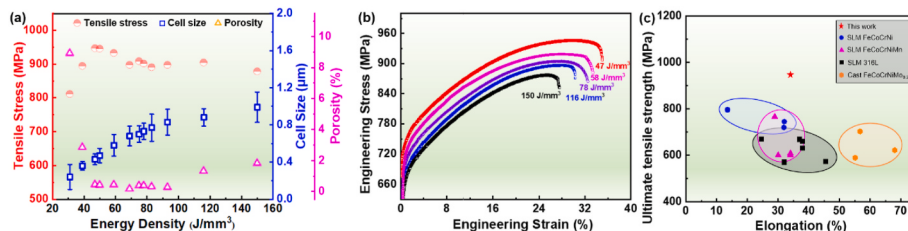


Fig. 10. (a) Variation of the yield strength, cellular substructure size, porosity and energy density of the SLMed FeCoCrNiMo_{0.2} HEA, (b) tensile stress-strain curves of the SLMed FeCoCrNiMo_{0.2} HEA under energy density from 47 J/mm³ to 150 J/mm³, (c) strength-ductility relationship of the SLMed FeCoCrNiMo_{0.2} HEA and other high-performance materials [12,14,26–40].

Table 5

Tensile properties of the SLMed FeCoCrNiMo_{0.2} HEA under different energy density.

Samples	Yield strength (MPa)	Ultimate tensile strength (MPa)	Elongation
47 J/mm ³	707	947	34 %
58 J/mm ³	693	919	33 %
77 J/mm ³	679	905	32 %
116 J/mm ³	657	896	30 %
150 J/mm ³	638	878	28 %

deformation microstructure in the fractured samples are shown in Fig. 11c–f. The bright-field (BF) TEM image in Fig. 11c exhibits remarkable dislocation trapping and retention mechanism at the cellular substructure boundaries, leading to the increase of dislocation density inside the cellular grains. Large area of planar slip bands, microbands and mechanical twins can be found (Fig. 11d–f), and these deformation substructures can substantially interact with cellular substructure to form a three-dimensional dislocation network. In short, the pinning of dislocations at the cellular substructure interface will produce a significant work hardening effect, thus improving the strength of the SLMed FeCoCrNiMo_{0.2} HEA, while the highly activated multiple deformation behavior is conducive to alleviating stress concentration and making additional contributions to the high plasticity.

4. Discussion

4.1. Microstructure evolution

Solidification theory, so-called “compositional supercooling”, is a widely accepted mechanism for cellular structures formed during AM process [10,41]. According to this theory, the cellular morphology is primarily influenced by two main parameters: the temperature gradient (G) and the solidification rate (R). The G/R ratio usually determines the solidification morphology of the cellular substructure in the molten pool. As the G/R ratio increases, the solidification morphology will gradually transform from equiaxed dendritic to columnar dendritic, cellular structure, and planar structure. In SLM, the high G/R ratio caused by extremely high cooling and solidification rates promotes the formation of cellular structures [10]. Meanwhile, the cooling rate (G × R) affects the cellular structure size, and a high G × R value will lead to a finer cellular substructure size. To establish the correlation between the energy density, temperature gradient, and solidification rate, the CFD method was performed to simulate the temperature field in the molten pool, and the temperature distribution diagram at each time was

obtained. Fig. 12a show the variation curves of temperature gradient and cooling rate under different energy densities. The result shows that as the energy density increases, the temperature gradient and cooling rate gradually decrease. At an energy density of 31 J/mm³, the temperature gradient and cooling rate are 29.26×10^6 K/mm and 14.12×10^6 K/s, respectively, while an increase in energy density to 150 J/mm³ results in a decrease in the temperature gradient to 3.65×10^6 K/mm and cooling rate to 0.32×10^6 K/s. The relationship between the cellular substructure size, temperature gradient, and solidification rate can be calculated by the following semiempirical relation: $d = 80(GR)^{-1/3}$ [42–44], where d is the cellular substructure size. Fig. 12b shows the comparison between the calculated cellular substructure size and the experimental value at different energy densities. It is obvious that the experimental values are consistent with the calculated values, and there is a positive correlation between the calculated cellular substructure size and energy density. This shows that the cellular substructure size can be predicted preferentially through temperature field simulation combined with empirical formula. In addition, Mo element segregation exists at the cellular substructure boundary, which becomes more obvious at a higher energy density. The solute segregation at cellular substructure boundary is a typical phenomenon during rapid solidification and is related to the equilibrium distribution coefficient of solute atoms during the solidification process [45]. Since the equilibrium distribution coefficient of Mo element is larger than that of other elements [19,20], there is obvious elemental segregation at the cellular substructure boundary. Numerous studies reported that the solute segregation mitigates with increasing cooling rate [45]. Fig. 12a shows that the cooling rate is a function of energy density, demonstrating a gradual decrease as the energy density increases. Therefore, it is reasonable the Mo element segregation became more obvious at the cellular substructure boundary with higher energy density, which is consistent with previous TEM EDS results.

4.2. Strengthening mechanism

The SLMed FeCoCrNiMo_{0.2} HEA exhibits enhanced mechanical properties than many high-performance materials prepared by traditional methods. The high strength of the SLMed materials is commonly attributed to the synergistic effects of various strengthening mechanisms [12,18], including grain boundary strengthening (σ_g), dislocation strengthening (σ_d) and segregation strengthening (σ_s). Therefore, the yield strength of the SLMed FeCoCrNiMo_{0.2} HEA can be calculated as follows:

$$\Delta\sigma_y = \Delta\sigma_f + \Delta\sigma_g + \Delta\sigma_d + \Delta\sigma_s \quad (1)$$

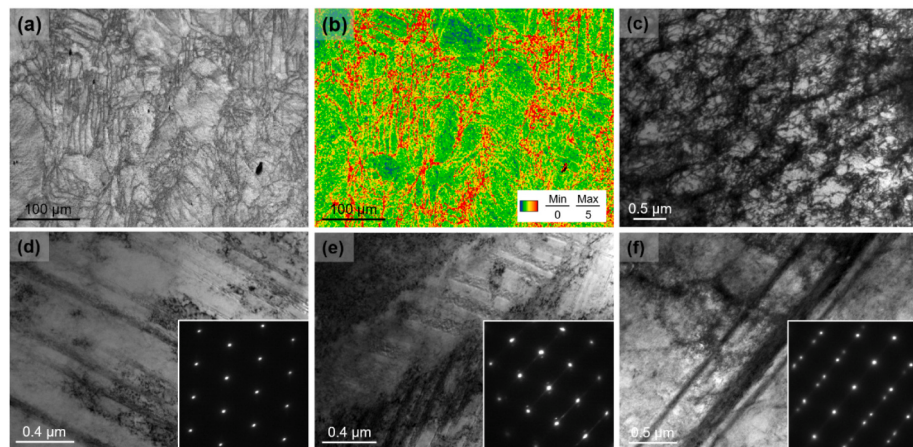


Fig. 11. Deformation microstructure of the FeCoCrNiMo_{0.2} HEA under energy densities of 47 J/mm³ (a) EBSD IQ; (b) KAM map; TEM images showing the (c) dislocation trapping, (d) dislocation slipping, (e) deformation microbanding, (f) mechanical twinning.

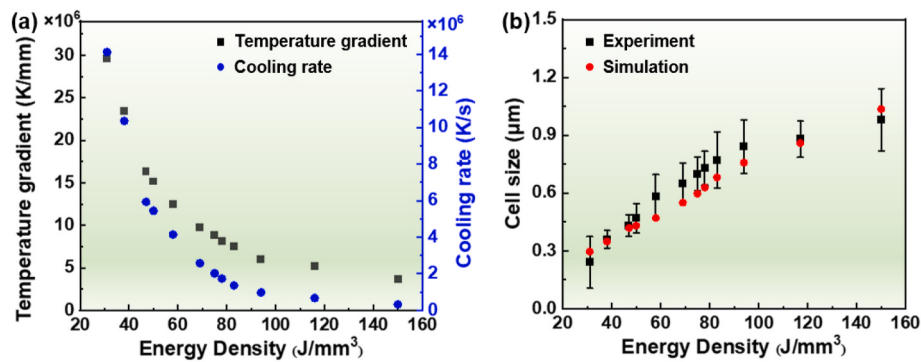


Fig. 12. Variation of (a) temperature gradient, cooling rate, and (b) cellular substructure size under different energy density.

where σ_f is the friction stress (adopted as 165 MPa [46]). The strength contribution from grain refinement (σ_g) is calculated using the Hall-Petch relationship [18]:

$$\Delta\sigma_g = Kd^{-1/2} \quad (2)$$

where K is the Hall-Petch coefficient (adopted as 226 MPa μm^{1/2} [47]) and d is the average grain size. For the SLMed FeCoCrNiMo_{0.2} HEA under energy density of 47 J/mm³, 78 J/mm³ and 150 J/mm³, d is 16.1 μm, 18.4 μm, and 20.4 μm, respectively, as illustrated in Fig. 6. Thus, the yield strengthening contribution from grain refinement is estimated to be 56.3 MPa, 53.7 MPa, and 50.1 MPa, respectively. The contribution of dislocation strengthening (σ_d) can be calculated based on the Taylor hardening equation [18]:

$$\Delta\sigma_d = MaGb\rho^{1/2} \quad (3)$$

where $M = 3.06$ is the Taylor factor [18], $\alpha = 0.2$ is the empirical constant [10], $G = 76$ GPa is the shear modulus [18], $b = 0.255$ nm is the Burgers vector [18], ρ is the dislocation density and can be calculated by the following formula: $\rho = 2\theta/\mu b$ [10], where θ is the average local misorientation value (Fig. 6), $u = 1.5$ μm is the EBSD scan unit length. As the energy density increases from 47 J/mm³ to 150 J/mm³, the GNDs for the SLMed FeCoCrNiMo_{0.2} samples gradually decrease from 1.39×10^{14} m⁻² to 0.81×10^{14} m⁻². It can be deduced that the ρ_{GNDs} increases with the decrease of the cellular substructure size. Therefore, the yield strengthening contributed by dislocations for the SLMed FeCoCrNiMo_{0.2} HEA under energy density of 47 J/mm³, 78 J/mm³ and 150 J/mm³ are estimated to be 140.1 MPa, 133.7 MPa, 106.7 MPa, respectively. The contribution of segregation strengthening can be calculated by the following equation:

$$\Delta\sigma_s = 0.57M(A\eta Y)^{1/3}(2\pi Gb/D)^{2/3} \quad (4)$$

where D is the average size of the cellular substructure (Fig. 6). A describes the amplitude of compositional segregation between the maximum solute concentration at the cellular substructure boundary and the minimum solute concentration at the cellular substructure core, as shown in Table 4 $\eta \approx 0.0007138$ at.% reflects the lattice mismatch [18]. $Y = 2G(1+v)/(1-v)$ represent the isotropic elastic assumption, where $v = 0.3$ is the Poisson's ratio [18]. Thus, the strength strengthening contribution from compositional segregation in the SLMed FeCoCrNiMo_{0.2} HEA under energy density of 47 J/mm³, 78 J/mm³ and 150 J/mm³ are estimated to be 299.9 MPa, 311.6 MPa, 320.7 MPa, respectively. Through the above analysis, the strength contribution of the SLMed FeCoCrNiMo_{0.2} HEA at different energy densities is summarized in Fig. 13, exhibiting a good agreement between the calculated results and the experimental data. It indicates that the segregation strengthening and dislocation strengthening stand out as the primary contributors to the SLMed FeCoCrNiMo_{0.2} HEA. In addition, the cellular substructure can act as a micro-heterogeneity consisting of hard cellular

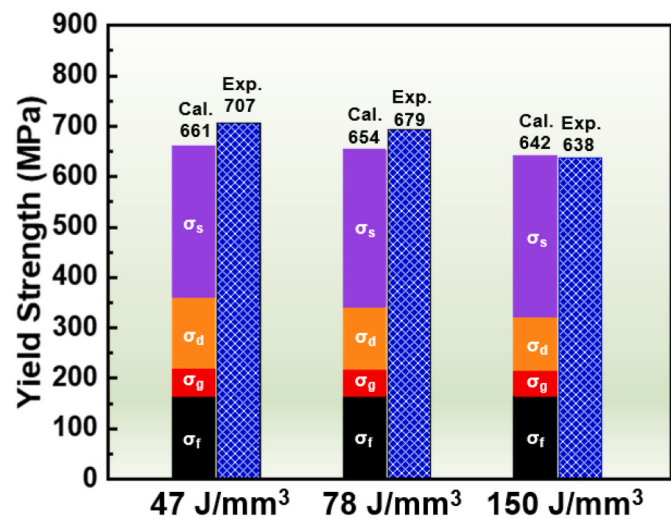


Fig. 13. Strength contribution of each strengthening mechanism for the SLMed FeCoCrNiMo_{0.2} HEA.

substructure boundaries and soft cellular substructure matrix [3,48], producing a high hetero-deformation induced (HDI) hardening. The Mo segregation along the cellular substructure boundaries is believed to promote both boundary dislocation density and strength [15,49,50], which is conducive to further enhancing the HDI stresses. This means that the cellular substructure size and the degree of Mo segregation at the boundaries directly impact the above strengthening mechanisms. Thus, controlling the microstructure of cellular substructures is an effective way to optimize the mechanical properties of SLM alloys.

5. Conclusions

In this work, FeCoCrNiMo_{0.2} HEA was fabricated by the SLM technology. The microstructural evolution of cellular substructures under different SLM process parameters and its effect on the mechanical properties were investigated. The main conclusions are as follows.

1. The SLMed FeCoCrNiMo_{0.2} HEA has a single-phase FCC structure, and shows a hierarchical structure of coarse grains and submicron cellular structures. Low energy density can promote the formation of fine cellular substructure size and homogeneous element distribution.
2. The increase in energy density causes a decrease in temperature gradient (G) and solidification rate (R), which consequently results in an increase in the cellular substructure size. The evolution of the cellular substructure size can be approximately described by the following formula: $d = 80(GR)^{-1/3}$.

3. The segregation strengthening and dislocation strengthening are considered as the main contributor to the yield strength of the SLMed FeCoCrNiMo_{0.2} HEA, which are directly affected by the size of cellular structures and segregation degree at the boundary of cellular structures.

CRediT authorship contribution statement

Ao Fu: Writing – original draft, Methodology, Investigation, Formal analysis. **Zhonghao Xie:** Writing – review & editing, Resources. **Jian Wang:** Formal analysis, Data curation. **Yuankui Cao:** Methodology, Investigation, Conceptualization. **Bingfeng Wang:** Resources, Conceptualization. **Jia Li:** Writing – review & editing, Formal analysis. **Qihong Fang:** Formal analysis, Data curation. **Xiaofeng Li:** Resources, Formal analysis. **Bin Liu:** Supervision, Project administration, Funding acquisition. **Yong Liu:** Supervision, Formal analysis.

Declaration of competing interest

The authors declare that they have no known competing financial interests or personal relationships that could have appeared to influence the work reported in this paper.

Data availability

No data was used for the research described in the article.

Acknowledgements

This study was financially supported by the National Natural Science Foundation of China [No. 52020105013], Natural Science Foundation of Hubei Province [No. 2022CFB894], and Natural Science Foundation of Hunan Province [No. 2022JJ40590].

References

- [1] T. DebRoy, H.L. Wei, J.S. Zuback, T. Mukherjee, J.W. Elmer, J.O. Milewski, A. M. Beese, A. Wilson-Heid, A. De, W. Zhang, Additive manufacturing of metallic components-process, structure and properties, *Prog. Mater. Sci.* 92 (2018) 112–224.
- [2] A. Fu, B. Liu, W.J. Lu, B. Liu, J. Li, Q.H. Fang, Z.M. Li, Y. Liu, A novel supersaturated medium entropy alloy with superior tensile properties and corrosion resistance, *Scripta Mater.* 186 (2020) 381–386.
- [3] J.M. Park, E.S. Kim, H. Kwon, P. Sathiyamoorthi, K.T. Kim, J.H. Yu, H.S. Kim, Effect of heat treatment on microstructural heterogeneity and mechanical properties of 1% C-CoCrFeMnNi alloy fabricated by selective laser melting, *Addit. Manuf.* 47 (2021) 102283.
- [4] A. Fu, B. Liu, F. Tan, Y. Cao, J. Li, B. Liu, Q. Fang, P.K. Liaw, Y. Liu, Structural damage and phase stability of cobalt-free FeCrNi medium-entropy alloy under high-fluence ion irradiation, *Appl. Surf. Sci.* 657 (2024) 159669.
- [5] A. Fu, B. Liu, Y.K. Cao, J. Wang, T. Liao, J. Li, Q.H. Fang, P.K. Liaw, Y. Liu, A novel cobalt-free oxide dispersion strengthened medium-entropy alloy with outstanding mechanical properties and irradiation resistance, *J. Mater. Sci. Technol.* 152 (2023) 190–200.
- [6] B. Sun, W. Lu, B. Gault, R. Ding, S.K. Makineni, D. Wan, C.H. Wu, H. Chen, D. Ponge, D. Raabe, Chemical heterogeneity enhances hydrogen resistance in high-strength steels, *Nat. Mater.* 20 (2021) 1629–1634.
- [7] F. Zhang, L.E. Levine, A.J. Allen, C.E. Campbell, E.A. Lass, S. Cheruvathur, M. R. Stoudt, M.E. Williams, Y. Idell, Homogenization kinetics of a nickel-based superalloy produced by powder bed fusion laser sintering, *Scripta Mater.* 131 (2017) 98–102.
- [8] C. de Formanoir, U. Paggi, T. Colebrants, L. Thijs, G. Li, K. Vanmeensel, B. Van Hooreweder, Increasing the productivity of laser powder bed fusion: influence of the hull-bulk strategy on part quality, microstructure and mechanical performance of Ti-6Al-4V, *Addit. Manuf.* 33 (2020) 101129.
- [9] J.H. Martin, B.D. Yahata, J.M. Hundley, J.A. Mayer, T.A. Schaeder, T.M. Pollock, 3D printing of high-strength aluminium alloys, *Nature* 549 (2017) 365–369.
- [10] H. Duan, B. Liu, A. Fu, J. He, T. Yang, C.T. Liu, Y. Liu, Segregation enabled outstanding combination of mechanical and corrosion properties in a FeCrNi medium entropy alloy manufactured by selective laser melting, *J. Mater. Sci. Technol.* 99 (2022) 207–214.
- [11] Y. Huang, Z. Xie, W. Li, H. Chen, B. Liu, B. Wang, Dynamic mechanical properties of the selective laser melting NiCrFeCoMo_{0.2} high entropy alloy and the microstructure of molten pool, *J. Alloys Compd.* 927 (2022) 167011.
- [12] Z.G. Zhu, Q.B. Nguyen, F.L. Ng, X.H. An, X.Z. Liao, P.K. Liaw, S.M.L. Nai, J. Wei, Hierarchical microstructure and strengthening mechanisms of a CoCrFeNiMn high entropy alloy additively manufactured by selective laser melting, *Scripta Mater.* 154 (2018) 20–24.
- [13] Z. Xie, A. Fu, H. Duan, B. Wang, X. Li, Y. Cao, B. Liu, Cryogenic mechanical behavior of a FeCrNi medium-entropy alloy fabricated by selected laser melting, *Intermetallics* 160 (2023) 107945.
- [14] Y. Brif, M. Thomas, I. Todd, The use of high-entropy alloys in additive manufacturing, *Scripta Mater.* 99 (2015) 93–96.
- [15][a] L. Liu, Q. Ding, Y. Zhong, J. Zou, J. Wu, Y.-L. Chiu, J. Li, Z. Zhang, Q. Yu, Z. Shen, Dislocation network in additive manufactured steel breaks strength-ductility trade-off, *Mater. Today* 21 (2018) 354–361.
- [15][b] R.X. Li, D.C. Kong, K.T. He, C.F. Dong, Superior thermal stability and strength of additively manufactured CoCrFeMnNi high-entropy alloy via NbC decorated sub-micro dislocation cells, *Scripta Mater.* 230 (2023) 115401.
- [16] Y. Chew, G.J. Bi, Z.G. Zhu, F.L. Ng, F. Weng, S.B. Liu, S.M.L. Nai, B.Y. Lee, Microstructure and enhanced strength of laser aided additive manufactured CoCrFeNiMn high entropy alloy, *Mater. Sci. Eng.* 744 (2019) 137–144.
- [17] T.R. Smith, J.D. Sugar, C. San Marchi, J.M. Schoenung, Strengthening mechanisms in directed energy deposited austenitic stainless steel, *Acta Mater.* 164 (2018) 728–740.
- [18] W. Li, Y. Huang, Z. Xie, H. Chen, W. Li, B. Liu, B. Wang, Mechanical property and cellular structure of an additive manufactured FeCoNiCrMo_{0.2} high-entropy alloy at high-velocity deformation, *J. Mater. Sci. Technol.* 139 (2023) 156–166.
- [19] S. Gao, Z. Hu, M. Duchamp, P.S.S.R. Krishnan, S. Tekumalla, X. Song, M. Seita, Recrystallization-based grain boundary engineering of 316L stainless steel produced via selective laser melting, *Acta Mater.* 200 (2020) 366–377.
- [20] Y.S. Hao, J. Li, X. Li, W.C. Liu, G.M. Cao, C.G. Li, Z.Y. Liu, Influences of cooling rates on solidification and segregation characteristics of Fe-Cr-Ni-Mo-N super austenitic stainless steel, *J. Mater. Process. Technol.* 275 (2020) 116326.
- [21] T. Kurzynowski, K. Gruber, W. Stoprya, B. Kuźnicka, E. Chlebus, Correlation between process parameters, microstructure and properties of 316L stainless steel processed by selective laser melting, *Mater. Sci. Eng.* 718 (2018) 64–73.
- [22] X. Luo, C. Yang, Z.Q. Fu, L.H. Liu, H.Z. Lu, H.W. Ma, Z. Wang, D.D. Li, L.C. Zhang, Y.Y. Li, Achieving ultrahigh-strength in beta-type titanium alloy by controlling the melt pool mode in selective laser melting, *Mater. Sci. Eng.* 823 (2021) 141731.
- [23] J. Wang, J. Zou, H. Yang, Z. Liu, S. Ji, High strength and ductility of an additively manufactured CrCoNi medium-entropy alloy achieved by minor Mo doping, *Mater. Sci. Eng.* 843 (2022) 143129.
- [24] D. Kong, C. Dong, S. Wei, X. Ni, L. Zhang, R. Li, L. Wang, C. Man, X. Li, About metastable cellular structure in additively manufactured austenitic stainless steels, *Addit. Manuf.* 38 (2021) 101804.
- [25] D. Lin, L. Xu, H. Jing, Y. Han, L. Zhao, F. Minami, Effects of annealing on the structure and mechanical properties of FeCoCrNi high-entropy alloy fabricated via selective laser melting, *Addit. Manuf.* 32 (2020) 101058.
- [26] F. Chen, F. Liu, Y.B. Tan, W. Shi, S. Xiang, Achieving excellent strength-ductility synergy via high density dislocation and nano-twinning in cryo-rolled FeCoCrNiMo_{0.2} high-entropy alloy, *J. Mater. Res. Technol.* 26 (2023) 2495–2507.
- [27] F. Chen, Y.B. Tan, S. Xiang, W. Shi, F. Liu, Enhanced strengthening effect via nano-twinning in cryo-rolled FeCoCrNiMo_{0.2} high-entropy alloys, *Mater. Sci. Eng.* 866 (2023) 144676.
- [28] W.H. Liu, Z.P. Lu, J.Y. He, J.H. Luan, Z.J. Wang, B. Liu, Yong Liu, M.W. Chen, C. T. Liu, Ductile CoCrFeNiMo_x high entropy alloys strengthened by hard intermetallic phases, *Acta Mater.* 116 (2016) 332–342.
- [29] Y. Hong, C. Zhou, S. Wagner, S. Schlabach, A. Pundt, L. Zhang, J. Zheng, Strain-induced twins and martensite: effects on hydrogen embrittlement of selective laser melted (SLM) 316 L stainless steel, *Corrosion Sci.* 208 (2022) 110669.
- [30] B. Li, Q. Yan, Y. Xu, Z. Liu, J. Zhang, F. Xuan, Additive manufacturing of ultrafine-grained austenitic stainless steel matrix composite via vanadium carbide reinforcement addition and selective laser melting: formation mechanism and strengthening effect, *Mater. Sci. Eng.* 745 (2019) 495–508.
- [31] E. Liverani, S. Toschi, L. Ceschin, A. Fortunato, Effect of selective laser melting (SLM) process parameters on microstructure and mechanical properties of 316L austenitic stainless steel, *J. Mater. Process. Technol.* 249 (2017) 255–263.
- [32] H.H. Alsalla, C. Smith, L. Hao, Effect of build orientation on the surface quality, microstructure and mechanical properties of selective laser melting 316L stainless steel, *Rapid Prototyp. J.* 24 (2018) 9–17.
- [33] J. Suryawanshi, K.G. Prashanth, U. Ramamurti, Mechanical behavior of selective laser melted 316L stainless steel, *Mater. Sci. Eng.* 696 (2017) 113–121.
- [34] Q. Chao, S. Thomas, N. Birbilis, P. Cizek, P.D. Hodgson, D. Fabijanic, The effect of post-processing heat treatment on the microstructure, residual stress and mechanical properties of selective laser melted 316L stainless steel, *Mater. Sci. Eng.* 821 (2021) 141611.
- [35] Y.K. Kim, J.H. Yu, H.S. Kim, K.A. Lee, In-situ carbide-reinforced CoCrFeMnNi high-entropy alloy matrix nanocomposites manufactured by selective laser melting: carbon content effects on microstructure, mechanical properties, and deformation mechanism, *Compos. B Eng.* 210 (2021) 108638.
- [36] B. Li, L. Zhang, Y. Xu, Z. Liu, B. Qian, F. Xuan, Selective laser melting of CoCrFeNiMn high entropy alloy powder modified with nano-TiN particles for additive manufacturing and strength enhancement: process, particle behavior and effects, *Powder Technol.* 360 (2020) 509–521.
- [37] R. Li, P. Niu, T. Yuan, P. Cao, C. Chen, K. Zhou, Selective laser melting of an equiatomic CoCrFeMnNi high-entropy alloy: processability, non-equilibrium microstructure and mechanical property, *J. Alloys Compd.* 746 (2018) 125–134.

- [38] D. Lin, L. Xu, X. Li, H. Jing, G. Qin, H. Pang, F. Minami, A Si-containing FeCoCrNi high-entropy alloy with high strength and ductility synthesized in situ via selective laser melting, *Addit. Manuf.* 35 (2020) 101340.
- [39] W. Wu, R. Zhou, B. Wei, S. Ni, Y. Liu, M. Song, Nanosized precipitates and dislocation networks reinforced C-containing CoCrFeNi high-entropy alloy fabricated by selective laser melting, *Mater. Char.* 144 (2018) 605–610.
- [40] R. Zhou, Y. Liu, C. Zhou, S. Li, W. Wu, M. Song, B. Liu, X. Liang, P.K. Liaw, Microstructures and mechanical properties of C-containing FeCoCrNi high-entropy alloy fabricated by selective laser melting, *Intermetallics* 94 (2018) 165–171.
- [41] K.G. Prashanth, J. Eckert, Formation of metastable cellular microstructures in selective laser melted alloys, *J. Alloys Compd.* 707 (2017) 27–34.
- [42] T.J. Lienert, J.C. Lippold, Improved weldability diagram for pulsed laser welded austenitic stainless steels, *Sci. Technol. Weld. Join.* 8 (2003) 1–9.
- [43] F. Mas, C. Tassin, F. Roch, M. Yesca, P. Todeschini, Y. Brechet, Growth morphologies and primary solidification modes in a dissimilar weld between a low-alloy steel and an austenitic stainless steel, *Metals* 8 (2018) 284.
- [44] Y. Zeng, L. Li, W. Huang, Z. Zhao, W. Yang, Z. Yue, Effect of thermal cycles on laser direct energy deposition repair performance of nickel-based superalloy: microstructure and tensile properties, *Int. J. Mech. Sci.* 221 (2022) 107173.
- [45] K. Karayagiz, L. Johnson, R. Seede, V. Attari, B. Zhang, X. Huang, S. Ghosh, T. Duong, I. Karaman, A. Elwany, R. Arróyave, Finite interface dissipation phase field modeling of Ni-Nb under additive manufacturing conditions, *Acta Mater.* 185 (2020) 320–339.
- [46] X. Chen, Y. Liang, Q. Wang, K. Dong, Y. Yang, S. Feng, X. Zhang, Y. Cai, Y. Peng, K. Wang, J. Kong, Introduction of nanoprecipitation into supersaturated CoCrFeNiMo_{0.5} alloy prepared by laser-powder bed fusion via microstructure tailoring to achieve excellent properties, *Scripta Mater.* 235 (2023) 115636.
- [47] W.H. Liu, Y. Wu, J.Y. He, T.G. Nieh, Z.P. Lu, Grain growth and the Hall-Petch relationship in a high-entropy FeCrNiCoMn alloy, *Scripta Mater.* 68 (2013) 526–529.
- [48] R.E. Kim, G.M. Karthik, A. Amanov, Y.-U. Heo, S.G. Jeong, G.H. Gu, H. Park, E. S. Kim, D.W. Lee, H.S. Kim, Superior gradient heterostructured alloys fabricated by laser powder bed fusion via annealing and ultrasonic nanocrystal surface modification, *Scripta Mater.* 230 (2023) 115422.
- [49] W. Zhang, J. Shen, J. Oliveira, H. Wang, S. Feng, N. Schell, B.J. Kooi, Y. Pei, Deformation processes of additively manufactured interstitial-strengthened high entropy alloy: in-situ high-energy synchrotron X-ray diffraction and microstructural appraisal, *Addit. Manuf.* 76 (2023) 103791.
- [50] Y. Zhong, L. Liu, S. Wikman, D. Cui, Z. Shen, Intragranular cellular segregation network structure strengthening 316L stainless steel prepared by selective laser melting, *Nucl. Mater.* 470 (2016) 170–178.